Rotor lattice model of ferroelectric large polarons

Georgios M. Koutentakis, Areg Ghazaryan, and Mikhail Lemeshko

Institute of Science and Technology Austria (ISTA), am Campus 1, 3400 Klosterneuburg, Austria

We present a minimal model of ferroelectric large polarons, which are suggested as one of the mechanisms responsible for the unique charge transport properties of hybrid perovskites. We demonstrate that short-ranged charge–rotor interactions lead to long-range ferroelectric ordering of rotors, which strongly affects the carrier mobility. In the nonperturbative regime, where our theory cannot be reduced to any of the earlier models, we reveal that the polaron is characterized by large coherence length and a roughly tenfold increase of the effective mass as compared to the bare mass. These results are in good agreement with other theoretical predictions for ferroelectric polarons. Our model establishes a general phenomenological framework for ferroelectric polarons providing the starting point for future studies of their role in the transport properties of hybrid organic-inorganic perovskites.

I. INTRODUCTION

The quasiparticle framework [1,2] offers a large degree of simplification in understanding the properties of interacting many-body systems. In particular, polaron models have been extremely successful in unveiling the transport properties of several classes of technologically relevant materials [3]. These include polar semiconductors [4–7] and transition metal oxides [8,9], as well as impurities in superfluid He [10–14] and ultracold atom Bose-Einstein condensates [15–20]. The general properties of these systems depend on the type of interaction providing the dressing of the impurities by their environment. Well-known types of electron–phonon coupling include the Fröhlich [21], Holstein [22,23], and Peierls [24–27] interactions, each of which gives rise to a distinct class of polaronic states. Recently, an alternative type of coupling has been proposed to explain the transport in hybrid organic-inorganic perovskites (HOIP) [28,29]. In this case, the carriers couple to the dipole moment fluctuations of their host, giving rise to the so-called ferroelectric polarons.

HOIP are highly relevant for applications, including their excellent performance as building blocks of solar cells [30–38]. However, their physical properties are notoriously complex due to their soft structure [39], ionic mobility [40,41], and the interplay between the rotational dynamics of the molecular cations and their structural and (photo)electric properties [42–45]. Earlier studies have attributed their transport properties to the collective orientation of organic cations [46] and spin-orbit coupling effects [47–49]. However, several recent studies [28,29,50–59] hold polarons responsible for the screening of carriers from charged defects, other carriers, and phonons, explaining the experimentally observed long carrier lifetimes and diffusion lengths [60]. Among these,

ferroelectric polarons are particularly promising [28,29], as they are expected to provide substantially enhanced screening compared to Fröhlich polarons [3,21]. However, the complex structure of the host material makes quantitative predictions for such quasiparticles difficult [28], hindering their unambiguous experimental verification. This necessitates the development of a reduced and general framework that can capture the key physical properties of these structures, as this would enable the identification of their relevance for explaining the transport properties of HOIP or possibly other molecular materials.

In this work we show that the formation of ferroelectric large polarons takes place already in a minimal model, where charge carriers interact with a one-dimensional array of planar rotors; see Fig. 1(a). The dipolar rotors model the reorientation dynamics of organic molecular cations, A^+, in the ABX_3 perovskite structure. Molecules interact with charge carriers hopping on the inorganic sublattice made of octahedral BX_6^-
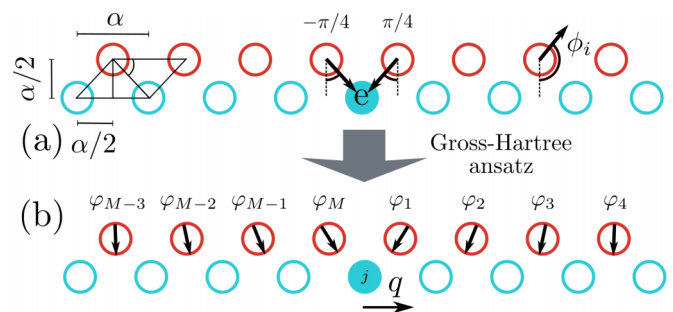

FIG. 1. (a) Tight binding model. Blue empty (filled) circles label empty (occupied) electron sites. Red circles show the dipole positions modeled by planar rotors. The distances between the sites and the orientations of the rotors/dipoles are also shown, where α is the lattice constant. (b) Illustration of the Gross-Hartree ansatz. The electron possesses quasimomentum, q, while the rotor states relative to it are described by the single-rotor states, $\varphi_j(\phi)$. Arrows show the orientations of the rotors.

cages, which we represent by discrete sites. Due to screening [61], we assume charge–dipole interactions to be short ranged and dipole–dipole interactions to be absent. As we demonstrate, this model captures the formation of local ~10 nm-sized ferroelectric order [58,62,63] and the crossover between a large light polaron (associated with ferroelectrically polarized dipoles) and a small heavy polaron regime characterized by charge carrier localization at the boundary of two misaligned ferroelectrically ordered domains [29,64].

This ferroelectric order significantly increases the effective mass of the carriers even within the light polaron regime, in accordance with the modest but not negligible mobilities observed in HOIP [60], but in contrast to other polaron models, e.g., the Holstein polaron, which predict much larger renormalization [65,66]. When the domain wall forms, the effective mass grows exponentially, suggesting high anisotropy of the mobilities and diffusion constants of large ferroelectric polarons in two and three dimensions. These transport anisotropies are the main signatures of the emergence of ferroelectric polarons. Note that such anisotropies along different crystallographic directions have been recently experimentally identified [67–69], hinting towards the relevance of our model for HOIP. The strength of our model is that our results depend only on the characteristic energy scales of tunneling, rotation, and interaction and thus our results hold for all cases where ferroelectric polarons emerge from local rotor–electron interactions irrespective of the underlying microscopic mechanisms.

Our work is structured as follows. Section II introduces our model, the relevant parameter scales for HOIP, and the variational Gross-Hartree (vGH) approach we employ to probe the properties of the system. Section III presents our main result, namely the crossover between the polarized ferroelectric phase and the state characterized by misaligned ferroelectric domain walls. In Sec. IV we evaluate coherence and transport properties of ferroelectric polarons within our model and analyze their parametric dependence. Section V presents the summary of our findings and provides perspectives for further studies. Appendix A outlines the Lang-Firsov approach applicable to our model and shows why the development of the vGH approach is important to address the polaron structures in HOIP. Describing the development and benchmarking of the latter approach is the focus of Appendix B. Finally, Appendix C provides the derivations of the perturbative results employed within Secs. III and IV.

II. EFFECTIVE MODEL

The Hamiltonian of our model, cf. Fig. 1(a), reads

$$
\begin{aligned}
\hat{H} = {} & -t \sum_{i=1}^{M} (\hat{a}_{i+1}^{\dagger} \hat{a}_i + \mathrm{H.c.}) - B \sum_{i=1}^{M} \frac{\partial^2}{\partial \phi_i^2} \\
& - V_0 \sum_{i=1}^{M} \hat{a}_i^{\dagger} \hat{a}_i \left[\cos\left(\phi_i + \frac{\pi}{4}\right) + \cos\left(\phi_{i-1} - \frac{\pi}{4}\right) \right],
\end{aligned}
$$

(1)

where $\hat{a}_i$ ($\hat{a}_i^{\dagger}$) are the electron annihilation (creation) operators, angles ϕ_i define the dipole orientations and B their rotational constants (in what follows we use the terms dipoles and rotors interchangeably), t is the tunneling rate of the electron, V_0 is

the electron–dipole interaction strength, and M is the number of rotors in the lattice. For simplicity we neglect the activation energy of molecular rotations, E_{act}, as its presence effectively inhibits rotor–electron interactions for $E_{\mathrm{act}} \gtrsim V_0$ [44,70]. Note that we employ periodic boundary conditions, i.e., $\hat{a}_{M+j}^{\dagger} = \hat{a}_j^{\dagger}$ and $\phi_{M+j} = \phi_j$, for all $j = 1, \ldots, M$. Although the model can be trivially extended to hole carriers by assuming $V_0 < 0$, here we focus on electrons, $V_0 > 0$. Note that the Hamiltonian (1) is quite general concerning the type of polar rotors and rotor–electron interactions. Thus similar models might be applicable in the case of fully inorganic perovskites, where the polar fluctuations are generated by deformations of inorganic cages containing Cs atoms [71].

Note that the Hamiltonian of Eq. (1) neglects some important effects occurring in HOIP materials, such as electron–phonon interactions [72,73] and induced polarization by halogen-metal hybridization [74,75], since these effects are not essential for ferroelectric polaron formation. Therefore, in this work we are not able to provide fair *quantitative* comparisons of our results with HOIP experiments nor explanations of the transport properties of HOIP alternative to ferroelectric polarons [76]. Nevertheless, the generality and extendability of our model opens the potential for future investigations, see Sec. V that addresses these questions.

In HOIP the molecular rotational energy $B \sim 1$ meV is the lowest energy scale since $V_0, t \sim 0.1$–1 eV [70,77]. To generate an appropriate rotor basis for $B \ll t$, we variationally optimize the state of the rotors relative to the electron, $\varphi_j(\phi)$, cf. Fig. 1(b), based on the following ansatz:

$$
|\Psi_q(\phi_1, \ldots, \phi_M)\rangle = \sum_{j=1}^{M} \frac{e^{i\frac{2\pi q}{M} j}}{\sqrt{M}} \prod_{k=1}^{M} \varphi_{I(k,j)}(\phi_k) \hat{a}_j^{\dagger} |0\rangle,
$$

(2)

where $|0\rangle$ and $\hat{a}_j$ are the electron vacuum and creation operators and $q = 0, \ldots, M - 1$ gives the quasimomentum of the polaron state. We will refer to this approach as the variational Gross-Hartree method (vGH). The indices of $\varphi_j(\phi)$ appearing in Eq. (2) read $I(k, j) = 1 + [(M + k - j) \bmod M]$ and are selected such that the rotor state depends only on the relative distance between the rotor and the electron. For instance, $\varphi_1(\phi)$ and $\varphi_M(\phi)$ refer to the state of the rotor on the right and left of the electron, respectively, independent of the position of the latter; cf. Fig. 1(b).

Note that, while the ansatz of Eq. (2) generalizes the basis generated via the Lang-Firsov transformation [3,78], see also Appendix A, as it allows for t-dependent modifications of the rotor state, it neglects dipole–dipole correlations. These are not expected to limit the applicability of vGH, since no direct interaction between dipoles appears in Eq. (1). Thus only dipole–dipole correlations mediated by the electron can take place, which result in small corrections in related polaron models (except for strong coupling) [79]. The applicability of the vGH approximation has been justified through comparison with exact diagonalization for small M; see Appendix B.

III. CROSSOVER FROM POLARIZED TO DOMAIN-WALL FERROELECTRIC ORDER

The order emerging in the rotor lattice can be elucidated by considering the rotor–electron correlation function at

distance j,

$$C_j(\phi) = M \int \cdots \int_{-\pi}^{\pi} \prod_{\substack{l=1 \\ l \neq j}}^{M} d\phi_l \langle \Psi_0(\phi_1, \ldots, \phi_{j-1}, \phi, \phi_{j+1}, \ldots, \phi_N) | \hat{a}_1^\dagger \hat{a}_1 | \Psi_0(\phi_1, \ldots, \phi_{j-1}, \phi, \phi_{j+1}, \ldots, \phi_N) \rangle$$

$$= |\varphi_j(\phi)|^2, \tag{3}$$

where the translational invariance of the system, see Eq. (2), allows us to fix the electron at the first site without loss of generality. The correlation function is shown in Fig. 2(a) for a small system with $M = 4$. In Fig. 2(b) we provide the average polarization of the rotors, $\langle \phi_j \rangle = \int_{-\pi}^{\pi} d\phi \, \phi C_j(\phi)$ for $M = 1024$, which is large enough to achieve convergence towards the $M \to \infty$ limit.

In the case of small $B = 10^{-3}t$, relevant for HOIP, we observe the emergence of two distinct interaction regimes. For $V_0 < 2t$ the rotors become strongly polarized towards the electronic lattice, $\phi \approx 0$, and an almost perfect ferroelectric order emerges [see Fig. 2(a) and the left panel of Fig. 2(c)]. Similarly, Fig. 2(b) shows $\langle \phi_j \rangle \approx 0$, for all j within this V_0 range. For $V_0 > 2t$, on the other hand, we observe domain formation in the rotor system; see Fig. 2(a) and the right panel of Fig. 2(c). The rotors to the left of the electron, $M/2 < j \leqslant M$, polarize with $\phi \approx \pi/4$, while the rotors at $1 \leqslant j \leqslant M/2$ polarize towards $\phi \approx -\pi/4$. Thus the electron acts as a ferroelectric domain wall, with rotors on each side of the electron pointing towards it. From Fig. 2(b) we can see that although this rotor ordering is local, it is quite extensive, involving ~ 50 rotors in each side of the electron. Note that this change in ferroelectric order with varying V_0 is gradual, of typical crossover character [80,81], as the rotors neighboring the electron from either side possess slightly different average orientations even for $V_0 < 2t$; see Fig. 2(b).

The interaction dependence of the local ferroelectric order, Fig. 2, provides an intuitive picture for the role of molecular dipole moments in the formation of polarons at ferroelectric domain bo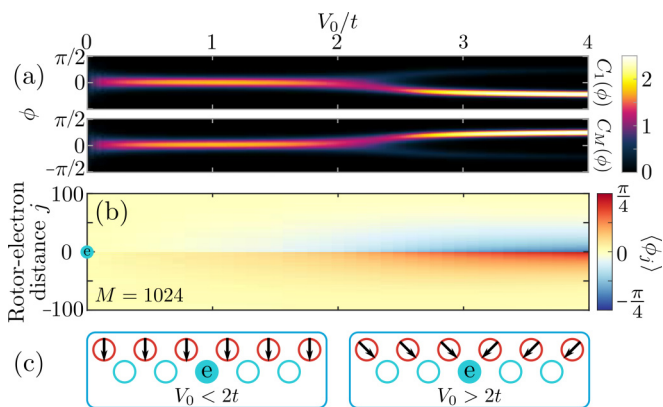undaries, proposed in Ref. [29]. That work suggests that the carriers are confined to and move along a two-dimensional ferroelectric domain wall, whereas the hopping perpendicular to it is much slower due to the distortion of the inorganic lattice. In our model this distortion corresponds to a reduced t along the distortion direction, resulting in an effectively higher V_0/t that can exceed the threshold for formation of ferroelectric domain walls, $V_0 \approx 2t$, in one dimension. In contrast, along the directions where no distortion takes place, V_0/t remains smaller than the threshold, which stabilizes an almost perfectly polarized rotor state.

The origin of the emerging order can be elucidated by examining the polaron energy, E_0. First, let us analyze its scaling with V_0; see Fig. 3(a). For small V_0, the polaron energy follows the perturbative result,

$$E_0 = -2t - \frac{V_0^2}{\sqrt{B(B + 4t)}} + O(V_0^2), \tag{4}$$

independent of B; see Appendix C. With increasing V_0, however, the energy of the polaron diverges from this scaling, with the strongest deviations observed for smaller B's. This behavior stems from the breakdown of perturbation theory for $V_0 > 2\sqrt{Bt}$, where the rotor–electron interaction creates a large number of rotor excitations.

The fact that the ferroelectric dressing of the electron observed in Fig. 2 takes place beyond the regime of validity of perturbation theory implies that it originates from the collective excitations of the rotor array and their coupling to the electron. Since the spectrum of rotors is different from that of harmonic oscillators, the nonperturbative physics of the ferroelectric polaron given by Eq. (1) is fundamentally different from the traditional models such as the Holstein polaron [3,22,23].

The fundamental difference between the $B < 10^{-2}t$ and $B \approx t$ regimes is directly observable by comparing the polaron energies for different B's near the crossover point, $V_0 \sim 2t$; see Fig. 3(b). For $B < 10^{-2}t$ and $V_0 < 2t$, the polaron energy features an almost linear decrease, $E_0 \approx -2t - \sqrt{2}V_0$,

FIG. 2. (a) Rotor-electron correlation function, $C_j(\phi)$, for $j = 1$ and $j = M = 4$, as a function of the electron–rotor interaction, V_0. The electron is fixed at the first site. (b) Average rotor orientation, $\langle \phi_j \rangle$, depending on the electron–rotor distance and V_0 for $M = 1024$. In both cases $B = 10^{-3}t$. (c) Schematic illustration of the ferroelectric orders involved.
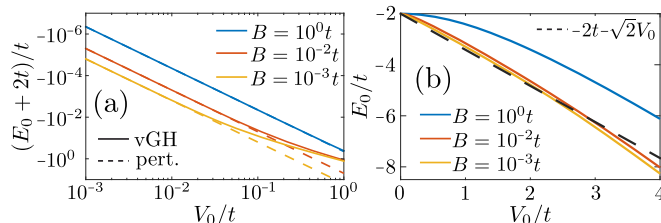

FIG. 3. (a), (b) Polaron energy, E_0, for different values of B as a function of V_0. Panel (a) compares the vGH results (solid lines) with perturbation theory (dashed lines). The dashed line in (b) is an eye guide to estimate E_0 (see the text). In all cases $M = 1024$.
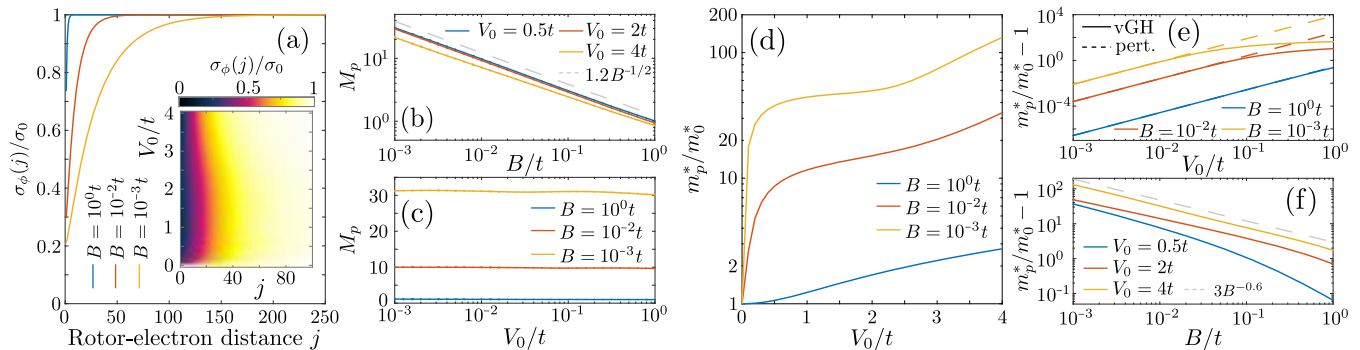
FIG. 4. (a) Variance of the rotor orientations, $\sigma_\phi(j)/\sigma_0$, for different B and $V_0/t = 0.5$. Inset: V_0 dependence of $\sigma_\phi(j)/\sigma_0$ for $B = 10^{-3}t$. (b), (c) Polaron size, M_p, derived from exponential fits of $\sigma_\phi(j)/\sigma_0$ as a function of (b) B and (c) V_0. (d), (e) The ratio of the polaron and free electron effective masses, m_p^*/m_0^* for different values of B, as a function of V_0. (e) Comparison of vGH results (solid lines) to perturbation theory (dashed lines). (f) The ratio m_p^*/m_0^* as a function of B. The dashed line in (b) and (f) serves as an eye guide to estimate the scaling with B. In all cases $M = 1024$.

stemming from strong polarization of the rotors ($\phi \approx 0$) in the vicinity of the electron. This results in the potential energy contribution $\sim V_0[\cos(\pi/4) + \cos(-\pi/4)] = -\sqrt{2}V_0$. For stronger interactions, $V_0 > 2t$, the polaron energy decreases faster than $\propto -\sqrt{2}V_0$ due to the domain-wall formation at the electron positions, which increases the rotor–electron attraction. For $B \sim t$, the behavior of the system changes and the polaron energy decreases quadratically. This is due to the large amount of energy required to create rotor excitations which hinders their polarization and the associated potential energy benefit, thereby precluding the formation of ferroelectric order.

IV. COHERENCE, TRANSPORT PROPERTIES, AND PARAMETER DEPENDENCE

Having discussed the basic properties of the polaronic states based on energetic arguments, let us focus on their coherence and transport properties and their relation to HOIP experiments. The polaron size, or, equivalently, the polaron coherence length, is associated with the extent of the ferroelectric order in the vicinity of the electron; see also Fig. 2(b). This property can be expressed through the variance of the rotor angle,

$$\sigma_\phi(j) = \left[\int_{-\pi}^{\pi} d\phi \, (\phi - \langle \phi_j \rangle)^2 C_j(\phi) \right]^{1/2}, \quad (5)$$

over the variance of the uniform distribution, $\sigma_0 = 2\pi/\sqrt{12}$. The value of $\sigma_\phi(j)/\sigma_0 = 1$ corresponds to a uniform density profile, where the dipoles are unaffected by the electron motion. The values $0 \leqslant \sigma_\phi(j)/\sigma_0 < 1$ correspond to the polarization of the jth rotor typical for ferroelectric order.

The localization of ferroelectric order is demonstrated by the exponential trend of $\sigma_\phi(j)/\sigma_0$ which rapidly saturates to unity as rotors far away from the electron remain not oriented; see Fig. 4(a). For fixed V_0, a larger number of rotors can be excited at smaller B, giving rise to a more extensive dressing cloud around the electron. Inversely, for $t = B$, the polaron is strongly localized in the vicinity of the electron, $j \to 0$, and thus cannot be called a large polaron. This is fully consistent with the energetic arguments presented above, cf. Fig. 3(b), and is further illustrated in Fig. 4(b). Here we use an

exponential fit,

$$\frac{\sigma_\phi(j)}{\sigma_0} = 1 + \left(\frac{\sigma_\phi(1)}{\sigma_0} - 1 \right) e^{-\frac{j-1}{M_p}}, \quad (6)$$

for $j < M/2$, to extract the polaron size M_p. We find that, almost independent of V_0, the polaron size grows as $\propto B^{-1/2}$ with decreasing B.

In contrast, for a constant B, the spatial extent of the polaron depends weakly on V_0; see the inset of Fig. 4(a), especially within the polarized regime, $V_0 < 2t$. This observation is confirmed by Fig. 4(c), which shows that M_p is independent of V_0 even for very small V_0's. This can be explained along the lines of perturbation theory: electron–rotor interactions result in virtual rotor excitations localized in the vicinity of the electron, whose momentum shifts from q to q'. These excitations are characterized by an energy B and thus a lifetime $\sim \hbar/B$. Consequently, the maximum distance between the electron and an excitation depends solely on the distribution of available q' and the excitation lifetime, both of which are independent of V_0 controlling the excitation probability. For $V_0 > 2t$, where the ferroelectric domain wall forms, the spatial extent of the polaron decreases by a factor of ~ 2; see the inset of Fig. 4(a). In this regime, the perturbative argumentation is invalid, since, as argued below, the electron becomes rigidly attached to its dressing cloud of rotor excitations. In summary, although the ferroelectric dressing is found to be large at the level of the unit cell, its spatial extent, $M_p \times \alpha \approx 30 \times 5$ Å ≈ 15 nm, is much smaller than the diffusion lengths of > 1 μm observed in HOIP experiments [82–84]. This implies that the semiclassical treatment of diffusion lengths, frequently used in the literature [60], is well justified also when ferroelectric polarons are present.

The ferroelectric order crucially affects the polaron mass, Fig. 4(d). Note that the mass scale for $V_0 = 0$ is $m_0^* = \hbar^2/(2t\alpha^2) \approx 0.15 \, m_e$ (for $\alpha \approx 5$ Å and $t \approx 1$ eV relevant for HOIP). For smaller B, the effective mass features a strong overall increase. For $B < 10^{-2}t$ the initial growth of $m_p^* = (\hbar^2/\alpha^2)(\partial^2 E_0/\partial q^2)^{-1}$ at smaller V_0 is followed by a plateau at $V_0 \sim t$. This can be rationalized by considering how m_p^* scales with B and V_0. From Fig. 4(e) we see that for small V_0 the

effective mass increases following the perturbative result,

$$\frac{m_p^*}{m_0^*} = 1 + \frac{B + 2t}{[B(B + 4t)]^{3/2}} V_0^2 + O(V_0^4), \tag{7}$$

see Appendix C, and saturates at larger V_0. The saturation of m_p^* can be thought of as an almost rigid attachment of the ferroelectric polarization cloud to the electron at strong interactions. For $B \sim t$ the attachment is precluded by rapid rotation of the rotors, resulting in no saturation of m_p^*. The scaling of m_p^* with B, Fig. 4(f), demonstrates significant deviations from the perturbative result, $m_p^*/m_0^* - 1 \propto B^{-3/2}$, in the region where the ferroelectric polaron forms, $V_0 \sim t \gg B$. The B scaling is found to be significantly less steep: $m_p^*/m_0^* - 1 \propto B^{-0.6}$ for $V_0 = 0.5t, 4t$, and $m_p^*/m_0^* - 1 \propto B^{-0.5}$ in the crossover region $V_0 = 2t$. Importantly, m_p^* is a decreasing function of B in all of the considered cases.

Thus, although the polaron for $V_0 < 2t$ is large, it features low but non-negligible mobility [85], $\mu \propto \tau/m_p^*$, which is consistent with HOIP experiments [60]. Here, τ corresponds to the mean scattering time which is large in HOIP [86] and is expected to increase due to polaron screening. The mean scattering time depends on the scattering cross section of the polaron with other polarons and charge defects and therefore its calculation requires a separate detailed study. For this reason below we comment on the dependence of μ on the effective mass. The effective mass predicted for the ferroelectric polaron, $m_p^* = 1.5–6m_e$ see Fig. 4(d), is large as compared to ARPES experiments [87], which yield effective masses close to the bare one, thereby challenging the polaron formation. However, recent experimental studies [88,89] have shown a ten- to hundredfold carrier mass increase after photoexcitation. This allows us to conjecture that ferroelectric polarons can only be formed after an initial relaxation step following photoexcitation, similar to the process described in Ref. [29]. Also, we would like to emphasize that the simultaneous power-law increase of the polaron size, M_p, and of its effective mass, m_p^*, with decreasing B, see Figs. 4(b) and 4(f), is the behavior that sets our model apart from the well-known Holstein and Fröhlich polarons, where larger effective masses are associated with smaller polaron sizes [3,22,23,90] or extremely heavy polarons with negligible mobilities [65,66]. This indicates that the framework of rotor lattices introduced here has the potential to explain the apparently contradicting features of carrier dynamics in HOIP.

For $V_0 > 2t$, m_p^* grows exponentially with V_0, Fig. 4(d), as a consequence of the reduced mobility due to the domain wall comoving with the electron. This is consistent with strong anisotropy of the effective mass along vs perpendicular to the ferroelectric domain wall once it forms [67–69]. Our results further suggest that the anisotropy in coherence length is much less pronounced; see the inset of Fig. 4(a). Thus the study of the relation between the coherence and mobility anisotropies might be important for the experimental detection of ferroelectric polarons in HOIP or other materials.

V. CONCLUSIONS AND OUTLOOK

In conclusion, we proposed a minimal, tractable, and extendable rotor lattice model describing the formation of

ferroelectric polarons [28,29,58]. The model captures several features of ferroelectric polarons such as their modest mobility but large coherence length. Furthermore, it provides intuition for the mechanism behind large polaron formation at ferroelectric domain boundaries, proposed in Ref. [29]. Our model lays the groundwork for realizing a top-down approach to the carrier dynamics in HOIP, complementary to the existing density functional theory studies [48,91–93] and other *ab initio* approaches [94–96].

Possible extensions include studying the phase diagram of the two-dimensional lattice system where signatures of carrier localization along different directions can be identified. The study of electron–hole interactions mediated by the rotors can elucidate the impact of the molecules on the observed long carrier lifetimes. Note that accounting for finite temperature, e.g., by using the techniques of Ref. [97], is quite straightforward. Moreover, our study suggests an interesting interplay of mobility inhomogeneity and exciton lifetime which might provide quantitative predictions for the diffusion length. Extensions to account for electron–phonon coupling can be done based on recent approaches [73,98]. This will allow one to fully capture the dressing of the carrier by the excitations present in HOIP materials [73,76], as well as to account for vibrational relaxation of the ferroelectric domain wall state [29]. In addition, studies that connect the abstract model parameters with realistic material properties will be crucial. The possibility of angulon formation affecting molecular mobility [99–103] and of the halogen-metal hybridization which can introduce polarization of the BX_6^- cages [74,75] might also be relevant for reliable modeling of HOIP properties with rotor lattice setups.

APPENDIX A: LANG-FIRSOV TRANSFORMATION

The Lang-Firsov transformation has been successfully used to describe polarons in the Holstein model [3,22,23,78]. Within the Lang-Firsov transformation one diagonalizes the Hamiltonian, $\hat{H}_{V_0 \to \infty}$ for $t = 0$, and then uses the unitary matrix $\hat{U}$ obtained by the diagonalization to obtain the hopping term in the transformed frame. Since in the case of the Holstein polaron the phonon–electron interaction has the simple form of a potential gradient, the operator $\hat{U}$ corresponds to a displacement operator for the phonons and therefore the transformation can be performed analytically.

In our case, however, $\hat{H}_{V_0 \to \infty}$ yields the Mathieu equation [104] and therefore the operator $\hat{U}$ has no simple analytic form. To describe how a pseudo-Lang-Firsov transformation can be performed in our case, let us assume that the electron is localized at position j. This allows us to diagonalize the rotor sector of the strong-coupling Hamiltonian by solving
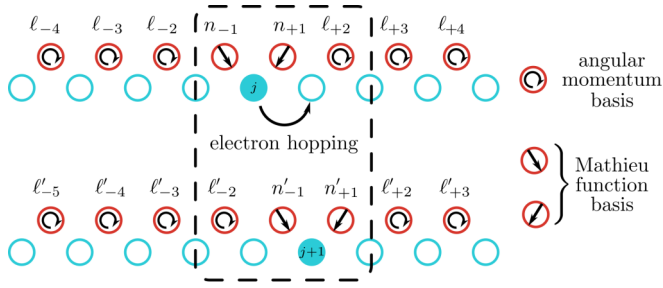
FIG. 5. Schematic illustration of the dipole-state-dependent correlated tunneling process described within the pseudo-Lang-Firsov transformation formalism. Blue empty (filled) circles label empty (occupied) electron sites. Red circles show the dipole positions modeled by planar rotors. The arrows and notation n_s, ℓ_s show the employed basis type (see legend) and state for the particular rotor site, $s = \pm 1, \ldots, \pm M/2$. The tunneling of the electron from site j to $j + 1$ couples the states of the rotors within the dashed rectangle, while for the remaining sites $\ell'_{s-1} = \ell_s$ holds.

the corresponding Mathieu and free-rotor equations. Note that within its eigenbasis the strong-coupling Hamiltonian reads

$$\hat{H}_{V_0 \to \infty} = \sum_{j=1}^{M} \sum_{k=1}^{\infty} \epsilon_k |j\rangle\langle j| \otimes |\Psi_{j,k}^{\text{rotors}}\rangle\langle\Psi_{j,k}^{\text{rotors}}|, \qquad \text{(A1)}$$

where ϵ_k, $|\Psi_{j,k}^{\text{rotors}}\rangle$ are the eigenenergies and eigenstates of the rotor system, respectively. Here we have used the fact that due to translational invariance ϵ_k is independent of the position of the electron. Furthermore, the electronic and rotor wave functions are in a product state but $|\Psi_{j,k}^{\text{rotors}}\rangle$ depends on the electron position, j, since only the dipoles next to the electron interact with it. The eigenstates of $\hat{H}_{V_0 \to \infty}$ form a complete basis and thus the identity operator can be expanded as $\hat{\mathbb{1}} = \sum_{j,k} |j\rangle\langle j| \otimes |\Psi_{j,k}^{\text{rotors}}\rangle\langle\Psi_{j,k}^{\text{rotors}}|$. This allows us to express the dipole–electron Hamiltonian of Eq. (1) as

$$\hat{H} = -t \sum_{j=1}^{\infty} \sum_{k,l} \left(\langle\Psi_{j,k}^{\text{rotors}}|\Psi_{j+1,l}^{\text{rotors}}\rangle |j\rangle\langle j+1| \right.$$
$$\otimes |\Psi_{j,k}^{\text{rotors}}\rangle\langle\Psi_{j+1,l}^{\text{rotors}}| + \text{H.c.})$$
$$+ \sum_{j=1}^{\infty} \sum_{k} \epsilon_k |j\rangle\langle j| \otimes |\Psi_{j,k}^{\text{rotors}}\rangle\langle\Psi_{j,k}^{\text{rotors}}|. \qquad \text{(A2)}$$

By appropriately selecting the many-rotor state indices k and l and by making use of the translational invariance we can simplify Eq. (A2) further; see Fig. 5. Here, the indices $n_{\pm 1}^k = 0, 1, \ldots$ parametrize the single particle eigenstate of the dipoles neighboring the electron, $|\psi_{n_{\pm 1}^k}^{\text{M}}\rangle$, which solves the corresponding Mathieu equation. Furthermore, $\ell_j^k = 0, \pm 1, \ldots$, with $j = \pm 2, \pm 3, \ldots$, are the indices of the angular momentum eigenstates, $\hat{L}_z |\psi_{\ell_j^k}^{\text{AM}}\rangle = \ell_j^k |\psi_{\ell_j^k}^{\text{AM}}\rangle$, for the dipoles further than the neighboring ones.

Note that within this framework each different many-rotor state k corresponds to a unique configuration $\{n_{\pm 1}^k, \ell_{\pm 2}^k, \ell_{\pm 3}^k, \ldots\}$ of the above mentioned single-rotor states. With these definitions the overlaps of the many-rotor

states contributing to tunneling read

$$\langle\Psi_{j,k}^{\text{rotors}}|\Psi_{j+1,l}^{\text{rotors}}\rangle = \left(\prod_{j'=-2,\pm 3,\pm 4,\ldots} \delta_{\ell_{j'}^k, \ell_{j'-1}^l} \right)$$
$$\times \langle\psi_{n_{-1}^k}^{\text{M}}|\psi_{\ell_{-2}^l}^{\text{AM}}\rangle\langle\psi_{n_{+1}^k}^{\text{M}}|\psi_{n_{-1}^l}^{\text{M}}\rangle$$
$$\times \langle\psi_{\ell_{+1}^k}^{\text{AM}}|\psi_{n_{+1}^l}^{\text{M}}\rangle \equiv O_{k,l}^R, \qquad \text{(A3)}$$

which are independent of j and thus translationally invariant. Also, $O_{kl}^L = \langle\Psi_{j+1,k}^{\text{rotors}}|\Psi_{j,l}^{\text{rotors}}\rangle = (O_{lk}^R)^*$ holds. By transforming to the momentum basis for the electron, $|q\rangle = \frac{1}{\sqrt{M}} \sum_{j=1}^{M} e^{i\frac{2\pi q}{M}j}|j\rangle$, Eq. (A2) reduces to $\hat{H} = \sum_{q=0}^{M-1} \hat{H}_q \otimes |q\rangle\langle q|$, with

$$\hat{H}_q = -t \sum_{k,l} \left(O_{k,l}^R e^{i\frac{2\pi q}{M}} |\Psi_k^{\text{rotors}}\rangle\langle\Psi_l^{\text{rotors}}| + \text{H.c.} \right)$$
$$+ \sum_{k} \epsilon_k |\Psi_k^{\text{rotors}}\rangle\langle\Psi_k^{\text{rotors}}| \qquad \text{(A4)}$$

describing the t-dependent effective interactions among the rotors when the electron lies in a particular $|q\rangle$ state. The energy of the kth many-rotor state is the sum of the energies of the constituent single-rotor states, namely

$$\epsilon_k = \frac{B}{4}\left[f_{n_{+1}^k}\left(\frac{2V_0}{B}\right) + f_{n_{-1}^k}\left(\frac{2V_0}{B}\right) \right] + B \sum_{j=2}^{M/2} \left[(\ell_j^k)^2 + (\ell_{-j}^k)^2 \right], \qquad \text{(A5)}$$

with $f_n(q)$ given in terms of the Mathieu characteristic numbers, namely $f_n(q) = a_n(q)$ for even n and $f_n(q) = b_n(q)$ for odd n.

For $B \gg t$ and $V_0 \sim B$ it follows that $t \ll \epsilon_k - \epsilon_{k'}$, for any k, k', and the t-mediated interaction does not affect the state of the rotors to a large degree. Thus the different tunneling channels $|\Psi_k^{\text{rotors}}\rangle$ do not interfere with one another. This defines different bands of the polaron with energies $\varepsilon_k(q) = \epsilon_k - 2t|O_{kk}^R| \cos[\frac{2\pi q}{M} + \arg(O_{k,k}^R)]$. For small $V_0 < B$, states with $n_{\pm 1}^k \neq n_{\pm 1}^{k'}$ but $\ell_j^k = \ell_j^{k'}$ for all $j = \pm 2, \pm 3, \ldots$ are coupled, implying local fluctuations of the rotor state in the vicinity of the electron, leading to interference of the above mentioned tunneling channels. However, the number of such coupled states is independent of M and the pseudo-Lang-Firsov approach can efficiently describe the polaron state.

In contrast, for $B \ll t$, which is the relevant case for applications in perovskites, $t \gg \epsilon_k - \epsilon_{k'}$ holds independent of V_0 at least in the cases where $n_{\pm 1}^k = n_{\pm 1}^{k'}$ and

$$\sum_{j=2}^{M} \left[(\ell_j^k)^2 - (\ell_j^{k'})^2 \right] + \sum_{j=2}^{M} \left[(\ell_{-j}^k)^2 - (\ell_{-j}^{k'})^2 \right] \ll \frac{t}{B}. \qquad \text{(A6)}$$

Therefore, in this case an extensive number of different $|\Psi_k^{\text{rotors}}\rangle$ states are strongly coupled by t-dependent effective interactions, provided that $V_0 \neq 0$ and thus $O_{kl}^R \neq \delta_{kl}$ hold. Consequently, the description of the system in this pseudo-Lang-Firsov basis becomes complicated. That is the main reason for the development of the vGH ansatz approach of Eq. (2), see also Appendix B, allowing for the construction of a Lang-Firsov-type basis that takes into account the effect of t-mediated interactions in a variational optimal manner.

APPENDIX B: DETAILS ON THE vGH APPROACH

1. vGH equations of motion

To variationally evaluate the polaron ground state of the rotor lattice model described by Eq. (1) we resort to the Dirac-Frenkel variational formalism, $E[\varphi_1(\phi;\tau), \ldots, \varphi_M(\phi;\tau)] = \langle \Psi(\tau)|\hat{H} - i\hbar\frac{\partial}{\partial\tau}|\Psi(\tau)\rangle$ [105,106]. The Dirac-Frenkel variational principle is a time-dependent variational technique, widely employed in quantum chemistry (see, e.g., Ref. [107]), that allows the dynamical explorations of complex systems in a variationally optimal manner in addition to their ground state properties. Note that we have chosen the Dirac-Frenkel variational principle solely based on the fact that our analysis becomes more transparent. Indeed, it can be shown that our variationally obtained equations of motion can be obtained by the Langrangian [108,109] or McLachlan [110] variational principles. This is a consequence of the fact that the Gross-Hartree ansatz of Eq. (2) is a linear combination of Hartree products and therefore it defines an analytic function, namely a linear combination of exponentials, due to the Thouless theorem [111,112].

The energy functional stemming from the Gross-Hartree ansatz reads

$$
\begin{aligned}
&E[\varphi_1(\phi;\tau), \ldots, \varphi_M(\phi;\tau)] \\
&= -t\Bigg(e^{i\frac{2\pi q}{M}} \prod_{j=1}^{M} \int d\phi\, \varphi_{j+1}^*(\phi;\tau)\varphi_j(\phi;\tau) \\
&\quad + e^{-i\frac{2\pi q}{M}} \prod_{j=1}^{M} \int d\phi\, \varphi_j^*(\phi;\tau)\varphi_{j+1}(\phi;\tau) \Bigg) \\
&\quad - B \sum_{j=1}^{M} \int d\phi\, \varphi_j^*(\phi;\tau)\frac{\partial^2}{\partial\phi^2}\varphi_j(\phi;\tau) \\
&\quad - i\hbar \sum_{j=1}^{M} \int d\phi\, \varphi_j^*(\phi;\tau)\frac{\partial}{\partial\tau}\varphi_j(\phi;\tau) \\
&\quad + V_0\Bigg[\int d\phi \cos\left(\phi+\frac{\pi}{4}\right)|\varphi_1(\phi;\tau)|^2 \\
&\quad + \int d\phi \cos\left(\phi-\frac{\pi}{4}\right)|\varphi_M(\phi;\tau)|^2 \Bigg] \\
&\quad + \sum_{j=1}^{M} \lambda_j(\tau)\left(1 - \int d\phi\, |\varphi_j(\phi;\tau)|^2\right), \quad \text{(B1)}
\end{aligned}
$$

with λ_j referring to the Lagrange multipliers ensuring the normalization of $\varphi_j(\phi;\tau)$.

The equations of motion are obtained via varying $E[\varphi_1(\phi;\tau), \ldots, \varphi_M(\phi;\tau)]$ with respect to $\varphi_j^*(\phi;\tau)$ and read

$$
\begin{aligned}
i\hbar\frac{\partial}{\partial\tau}\varphi_j(\phi;\tau) &= [\hat{H}_j - \lambda_j(\tau)]\varphi_j(\phi;\tau) \\
&\quad - t\, e^{i\frac{2\pi q}{M}}\mathcal{T}_{jL}(\tau)\varphi_{j-1}(\phi;\tau) \\
&\quad - t\, e^{-i\frac{2\pi q}{M}}\mathcal{T}_{jR}(\tau)\varphi_{j+1}(\phi;\tau), \quad \text{(B2)}
\end{aligned}
$$

where $\hat{H}_j = -B\frac{\partial^2}{\partial\phi^2} + \delta_{j1}V_0\cos(\phi+\frac{\pi}{4}) + \delta_{jM}V_0\cos(\phi-\frac{\pi}{4})$ and the nonlinearity of the above equations stems from the mean-field tunneling couplings $\mathcal{T}_{jL}(\tau) =$

$\prod_{k\neq j}\int d\phi\, \varphi_k^*(\phi;\tau)\varphi_{k-1}(\phi;\tau)$ and $\mathcal{T}_{jR}(\tau) = \prod_{k\neq j}\int d\phi\, \varphi_k^*(\phi;\tau)\varphi_{k+1}(\phi;\tau)$, which are analogous to the $O_{k,l}^R$ appearing in the Lang-Firsov formalism; see Eq. (A3). Finally, in order to calculate the Langrange coefficients we demand that the $\varphi_j(\phi;t)$ functions remain normalized and employ the fact that the Hamiltonian is Hermitian to obtain

$$
\begin{aligned}
\lambda_j(\tau) &= \int d\phi\, \varphi_j^*(\phi;\tau)\hat{H}_j\varphi_j(\phi;\tau) \\
&\quad - t\big(e^{i\frac{2\pi q}{M}}\mathcal{T}_L(\tau) + e^{-i\frac{2\pi q}{M}}\mathcal{T}_R(\tau)\big), \quad \text{(B3)}
\end{aligned}
$$

where $\mathcal{T}_L(\tau) = \prod_{k=1}^{M}\int d\phi\, \varphi_k^*(\phi;\tau)\varphi_{k-1}(\phi;\tau)$ and $\mathcal{T}_R(\tau) = \prod_{k=1}^{M}\int d\phi\, \varphi_k^*(\phi;\tau)\varphi_{k+1}(\phi;\tau)$. The above expression implies that $\lambda_j(t)$ is always real and thus, even if the $\lambda_j(\tau)\varphi_j(\phi;\tau)$ term of Eq. (B2) is neglected, the magnitude of the single rotors' states is conserved, since

$$
\frac{d}{d\tau}\left[\int d\phi\, |\varphi_j(\phi;\tau)|^2\right] = \frac{2}{\hbar}\mathcal{I}(\lambda_j(\tau)) = 0. \quad \text{(B4)}
$$

Therefore, the Lagrange multipliers are not *per se* needed for dynamical investigations, e.g., to study polaron dynamics.

However, herewith we are mainly interested in the ground state properties of the system, which can be calculated by imaginary time propagation. Within this approach we perform the transformation $\tau \to -i\tau$ in Eq. (B2) resulting in a diffusion equation. This equation has an important property that the energy of the propagated state monotonically decreases in time according to $\sim e^{-(E(\tau)-E_0)\tau}$, where E_0 is the true ground state energy, and therefore the ground state is obtained in the limit of $\tau \to \infty$. In our implementation we perform finite imaginary time propagation up to the point that the right-hand side of Eq. (B2) is smaller than a tolerance of $10^{-12}B$, thus ensuring that the final state is stationary with a confidence comparable to the machine error.

2. Comparison with exact diagonalization for small systems

As discussed in Sec. II, the vGH ansatz of Eq. (2) neglects dipole–dipole correlations stemming from the effective rotor–rotor interactions due to electron tunneling. We expect that these corrections are small and as such they do not significantly affect the behavior of the system. Accounting for such correlations is a nontrivial task, as they involve multiple configurations of rotor states. In the absence of approximations, i.e., within exact diagonalization (ED), there are $\mathcal{M}^M$ such different configurations, where $\mathcal{M}$ is the number of single-rotor states considered. To ensure the convergence of the ED, $\mathcal{M}$ should be large enough so that the observables of interest become independent of its increase. This implies an exponential increase of the numerical complexity with the system size and consequently the ED treatment is computationally prohibitive for large M. Therefore, to obtain a numerical estimate of the error in the vGH results due to neglecting these correlations, we have to rely on small systems where ED is feasible.
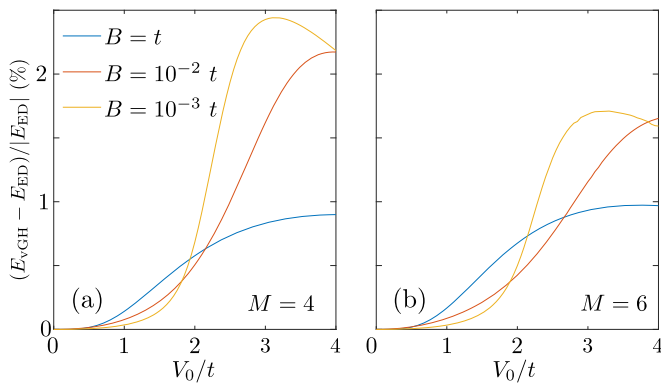
FIG. 6. Percentage deviation of the ground state energy within the ED and vGH approaches, $(E_{\mathrm{vGH}} - E_{\mathrm{ED}})/|E_{\mathrm{ED}}|$, as a function of V_0 for (a) $M = 4$ and (b) $M = 6$ for different B/t (see legend).

FIG. 7. Rotor–electron correlation functions, $C_j(\phi)$, with $j = 1, \ldots, M$ (see row labels) as a function of V_0 within the exact diagonalization (left column) and vGH (right column) approaches. In both cases a small system with $M = 4$ and $B = 10^{-3}t$ is considered.

In particular, for our ED calculations we used $\mathcal{M} = 21$ resulting in 194 481 and 85 776 121 rotor configurations for $M = 4$ and $M = 6$, respectively. The individual single-rotor states correspond to the eigenstates of the $\hat{L}_z$ operator, with eigenvalues $|\ell_z| < (\mathcal{M} - 1)/2$. This choice of the many-rotor basis is sufficient for the ED energies to converge at the 10^{-5} level.

The percentile deviation of the vGH and ED ground state energies, $(E_{\mathrm{vGH}} - E_{\mathrm{ED}})/|E_{\mathrm{ED}}|$, is shown in Fig. 6. Here it is verified that the energy contribution of the rotor-rotor correlations is indeed small, lying in the few % range. In particular, we observe that the deviation is the largest in the interaction regime where the ferroelectric domain-wall forms, $V_0 > 2t$. In this regime $(E_{\mathrm{vGH}} - E_{\mathrm{ED}})/|E_{\mathrm{ED}}|$ additionally exhibits an increasing tendency with decreasing B. In contrast, the rotor-rotor correlations seem to become less significant as B decreases for interactions supporting the polarized state, $V_0 < 2t$. Our results further suggest that the correlation corrections become less pronounced for increasing M, compare Fig. 6(a) and Fig. 6(b), provided that $B \leqslant 10^{-2}$.

To demonstrate that our results are robust to the inclusion of rotor-rotor correlations, Fig. 7 compares $C_j(\phi)$ within ED and vGH. The behavior of $C_j(\phi)$ for the different approaches is nearly identical qualitatively, but there are a few notable quantitative differences. In particular, while both approaches capture the crossover from the almost perfectly ferroelectrically polarized to the domain-wall state, the threshold shifts to a lower V_0 value within ED. In addition, within the $V_0 > 2t$ where the domain-wall forms, vGH shows significantly larger values of $C_2(\phi)$ and $C_3(\phi)$ than ED for $\phi = \pi/4$ and $\phi = -\pi/4$, respectively. The above indicates that the overlap of adjacent rotors decreases when accounting for rotor-rotor correlations, which can be associated with a reduction of the mean-field tunneling integrals $\mathcal{T}_{jL}$ and $\mathcal{T}_{jR}$. Therefore, rotor–rotor correlations might induce further increase of the polaron effective mass when the domain wall forms.

In conclusion, rotor–rotor interactions do not substantially alter the polaron state; however, properly accounting for them might be beneficial for obtaining high-accuracy predictions for the polaronic properties.
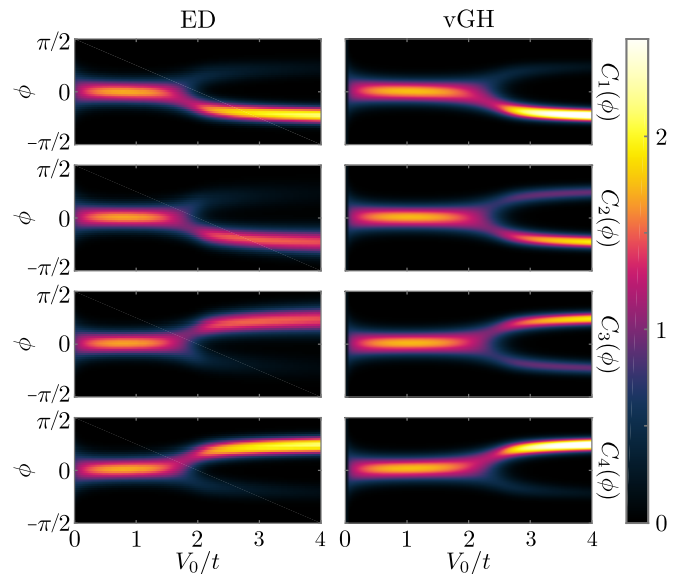
APPENDIX C: PERTURBATIVE TREATMENT OF THE ROTOR-LATTICE HAMILTONIAN

In order to get an insight into the polaron state let us now consider the case where V_0 is much smaller than the rest of the system parameters and can thus be treated perturbatively. To this end, within this section we apply the Brillouin-Wigner (BW) perturbation theory [113], which as we will see below can be used to infer the results of other commonly used theoretical approaches in polaron physics.

Note that for $V_0 = 0$ the rotational and translational degrees of freedom decouple and as such we can define their eigenstates as $|\mathbf{m} = (m_1, m_2, \ldots, m_M)\rangle$ and $|k\rangle$, respectively. Here, k denotes the quasimomentum of the electron. The corresponding eigenenergies are $\epsilon_{\mathbf{m}}^{\mathrm{rot}} = B \sum_{i=1}^{M} m_i^2$ and $\epsilon_k^{\mathrm{tr}} = -2t \cos(k)$. The interaction Hamiltonian acting here as the perturbation, see also Eq. (1), reads

$$\hat{H}_I = -V_0 \sum_{j=1}^{M} \hat{a}_j^\dagger \hat{a}_j \cos\left(\phi_j + \frac{\pi}{4}\right)$$
$$- V_0 \sum_{j=1}^{M} \hat{a}_j^\dagger \hat{a}_j \cos\left(\phi_{j-1} - \frac{\pi}{4}\right). \quad \text{(C1)}$$

Given that all interaction terms appearing in the rotor-electron interaction Hamiltonian are of the form $\hat{a}_n^\dagger \hat{a}_n e^{\pm i\phi_j}$, implies that only the states $|k; \mathbf{m}\rangle$ and $|k; \mathbf{m} \pm \hat{\mathbf{e}}_j\rangle$, where $\hat{\mathbf{e}}_j$ is the unit vector of the jth axis, are directly coupled by the interaction. Therefore, within the second-order BW perturbation theory the wave function expansion reads

$$|\Psi(k, \mathbf{m})\rangle = \alpha_{k,\mathbf{m}} |k; \mathbf{m}\rangle + \sum_{k'} \sum_{j=1}^{M} (\beta_{k,k',\mathbf{m},j} |k'; \mathbf{m} + \hat{\mathbf{e}}_j\rangle$$
$$+ \gamma_{k,k',\mathbf{m},j} |k'; \mathbf{m} - \hat{\mathbf{e}}_j\rangle), \quad \text{(C2)}$$

where the wave function coefficients $a_{k,\mathbf{m}}$, $\beta_{k,k',\mathbf{m},j}$, and $\gamma_{k,k',\mathbf{m},j}$ are expressed in terms of the total energy of the system, E, as

$$\alpha_{k,\mathbf{m}} = \sqrt{Z},$$

$$\beta_{k,k',\mathbf{m},j} = -\sqrt{Z} \frac{\langle k';\mathbf{m}+\hat{\mathbf{e}}_j|\hat{H}_I|k;\mathbf{m}\rangle}{\epsilon_{k'}^{\mathrm{tr}} + \epsilon_{\mathbf{m}+\hat{\mathbf{e}}_j}^{\mathrm{rot}} - E},$$

$$\gamma_{k,k',\mathbf{m},j} = -\sqrt{Z} \frac{\langle k';\mathbf{m}-\hat{\mathbf{e}}_j|\hat{H}_I|k;\mathbf{m}\rangle}{\epsilon_{k'}^{\mathrm{tr}} + \epsilon_{\mathbf{m}-\hat{\mathbf{e}}_j}^{\mathrm{rot}} - E}. \tag{C3}$$

Note that the wave function renormalization of the perturbative state is performed via the insertion of the polaron residue, Z. This factor is calculated by demanding that $\langle \Psi(k,\mathbf{m})|\Psi(k,\mathbf{m})\rangle = 1$. The above lead to the following equation for the polaron energy:

$$E = \epsilon_k^{\mathrm{tr}} + \epsilon_{\mathbf{m}}^{\mathrm{rot}} - \Sigma_{k,\mathbf{m}}(E), \tag{C4}$$

where $\Sigma_{k,\mathbf{m}}(E)$ denotes the so-called self-energy of the system

$$\Sigma_{k,\mathbf{m}}(E) = \sum_{k'} \sum_{j=1}^{M} \left(\frac{|\langle k;\mathbf{m}|\hat{H}_I|k';\mathbf{m}+\hat{\mathbf{e}}_j\rangle|^2}{\epsilon_{k'}^{\mathrm{tr}} + \epsilon_{\mathbf{m}+\hat{\mathbf{e}}_j}^{\mathrm{rot}} - E} + \frac{|\langle k;\mathbf{m}|\hat{H}_I|k';\mathbf{m}-\hat{\mathbf{e}}_j\rangle|^2}{\epsilon_{k'}^{\mathrm{tr}} + \epsilon_{\mathbf{m}-\hat{\mathbf{e}}_j}^{\mathrm{rot}} - E} \right). \tag{C5}$$

Importantly, Eq. (C4) can also be derived by using Eq. (C2) as a variational ansatz and minimizing the energy functional $E = \langle \Psi(k,\mathbf{m})|\hat{H}|\Psi(k,\mathbf{m})\rangle$, under the constraint of normalized $|\Psi(k,\mathbf{m})\rangle$. This approach is commonly referred to as the Chevy ansatz approach [114] and has applications in Fermi polarons emerging in ultracold atomic Fermi gases [115–118]. Since Eq. (C4) is derived within BW perturbation theory, it features, in principle, multiple solutions corresponding to the analytic continuation of each of the participating $V_0 = 0$ eigenstates, $|k;\mathbf{m}\rangle$. In addition, since it can be derived within the Chevy ansatz, the lowest in energy solution of Eq. (C4) is an upper bound to the true ground state energy of the system, corresponding to the polaron. Within this framework we can identify several polaronic properties such as the above mentioned residue Z, the polaron energy $E_p = E - \epsilon_k^{\mathrm{tr}} = -\Sigma_{k,\mathbf{0}}(E_p + \epsilon_k^{\mathrm{tr}})$, and the polaronic effective mass $m^* = (\frac{\partial^2 E}{\partial k^2})^{-1}$.

To proceed note that the matrix elements of $\hat{H}_I$ read

$$\langle k';\mathbf{m}+\hat{\mathbf{e}}_j|\hat{H}_I|k;\mathbf{m}\rangle = -\frac{V_0 e^{i(k-k')(j-\frac{1}{2})}}{M} \cos\left(\frac{k-k'}{2} + \frac{\pi}{4}\right),$$

$$\langle k';\mathbf{m}-\hat{\mathbf{e}}_j|\hat{H}_I|k;\mathbf{m}\rangle = -\frac{V_0 e^{i(k-k')(j-\frac{1}{2})}}{M} \cos\left(\frac{k-k'}{2} - \frac{\pi}{4}\right), \tag{C6}$$

and, consequently, the self-energy for $\mathbf{m} = \mathbf{0}$ reads

$$\Sigma_{k,\mathbf{0}}(E) = \frac{V_0^2}{M} \sum_{k'} \frac{1}{B - E - 2t \cos k'}$$

$$= \begin{cases} -\frac{V_0^2}{\sqrt{(B-E)^2 - 4t^2}} & \text{for} \quad E > B + 2t, \\ \frac{V_0^2}{\sqrt{(B-E)^2 - 4t^2}} & \text{for} \quad E < B - 2t. \end{cases} \tag{C7}$$

In the intermediate range $B - 2t < E < B + 2t$ the self-energy becomes imaginary, indicating that no polaron exists in this regime. This stems from the extrapolation to the thermodynamic limit by substituting $\sum_k \to \frac{M}{2\pi}\int dk$. In this limit, the bands corresponding to the rotor excitations become a continuum of states in the energy interval $B - 2t < E < B + 2t$. Thus any discrete state that couples to this continuum of excitations becomes exponentially damped in time explaining its imaginary self-energy.

Having an exact expression for $\Sigma_{k,\mathbf{m}}(E)$ we can identify the minimum of the polaron band. To find the minimum of the energy we differentiate E with respect to k for $E < B - 2t$, yielding

$$\left(1 + \frac{\partial \Sigma_{k,\mathbf{0}}}{\partial E} \right) \frac{dE}{dk} = \frac{d\epsilon_k^{\mathrm{tr}}}{dk} - \frac{\partial \Sigma_{k,\mathbf{0}}}{\partial k}. \tag{C8}$$

Therefore, $k = 0$ is an extremal point since $\partial\Sigma_{k,\mathbf{0}}/\partial k = 0$, $d\epsilon_k^{\mathrm{tr}}/dk = 0$, and $\partial\Sigma_{k,\mathbf{0}}/\partial E > 0$. Using the above and by differentiating once more with k we find

$$\left(1 + \frac{\partial \Sigma_{k,\mathbf{0}}}{\partial E} \right) \frac{d^2 E}{dk^2} = \frac{d^2 \epsilon_k^{\mathrm{tr}}}{dk^2}. \tag{C9}$$

Thus we conclude that $k = 0$ is the minimum of the polaron band for all values of B, V_0, and $t > 0$.

The above allows us to evaluate the polaron characteristics by focusing on $k = 0$. First, the polaron energy is the lowest in energy solution of the algebraic equation

$$E_p = -\frac{V_0^2}{\sqrt{(B + 2t - E_p)^2 - 4t^2}}, \tag{C10}$$

which up to fourth order in V_0 yields

$$E_p = -\frac{V_0^2}{\sqrt{B(B+4t)}} + \frac{B+2t}{B^2(B+4t)^2} V_0^4 + O(V_0^6). \tag{C11}$$

By substituting $E = \epsilon_k^{\mathrm{tr}}$ in the right hand size of Eq. (C4) it can be shown that the above expansion up to order $\propto V_0^2$ agrees with the second-order Rayleigh-Schrödinger perturbation theory. For this reason we compare the second order correction with the vGH results in Sec. III; see Eq. (4). Note that here by employing Eq. (C10) it can be proven that within the Chevy ansatz $E_p + V_0^2/\sqrt{B(B+4t)} > 0$ holds for all values of the parameters B, V_0, and t. In addition, explicit numerical solutions of Eq. (C10), see Fig. 8, show that the vGH value of E_p is always significantly smaller than the Chevy ansatz result. demonstrating that the vGH approach is a significant improvement to the Chevy ansatz.

Nevertheless, Eq. (C11) indicates that the characteristic interaction scale obtained via BW perturbation theory is $V_0/\sqrt{B(B+4t)}$. Indeed, it can be seen that the vGH results
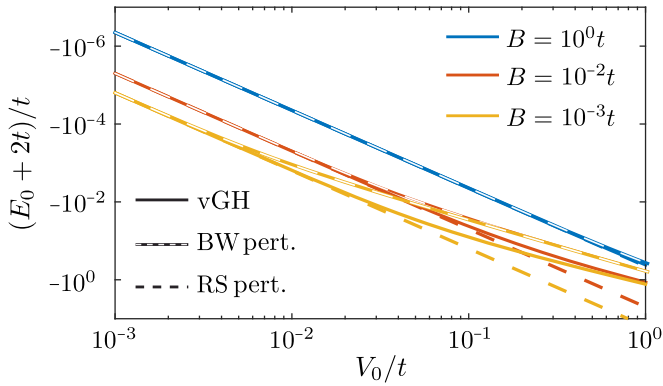
FIG. 8. (a), (b) Comparison of the polaron energy, E_0, obtained by the vGH approach and Brillouin-Wigner and Rayleigh-Schrödinger perturbation theory for different values of B as a function of V_0. The vGH results correspond to $M = 1024$, while perturbation theory refers to $M \to \infty$.

presented in Sec. III begin to deviate when this dimensionless scale becomes of order ~ 1. Finally, let us derive the value of the effective mass within the above-mentioned perturbation theories. Within the BW perturbation theory/Chevy ansatz the

effective mass is a function of the polaron energy, E_p,

$$\frac{m_p^*}{m^*} = 1 - \frac{B + 2t - E_p}{V_0^4} E_p^3. \qquad (C12)$$

And thus a substitution of Eq. (C11) to Eq. (C12) yields up to fourth order in V_0:

$$\frac{m_p^*}{m_p} = 1 + \frac{B + 2t}{[B(B + 4t)]^{3/2}} V_0^2$$
$$- \frac{2(B^2 + 4Bt + 6t^2)}{B^3(B + 4t)^3} V_0^4 + O(V_0^6). \qquad (C13)$$

The same evaluation within the Rayleigh-Schrödinger perturbation theory results in

$$\frac{m_p^*}{m_p} = 1 + \frac{2t}{[B(B + 4t)]^{3/2}} V_0^2 + O(V_0^4). \qquad (C14)$$

Therefore, the results for the effective mass agree up to quadratic order for $B \ll t$. In the main text we employ the second-order correction within BW, Eq. (C13), as the perturbative result to compare with vGH; see Eq. (7). The BW result provides improved agreement with vGH even in the case of $B = t$.

[1] L. D. Landau, On the motion of electrons in a crystal lattice, Phys. Z. Sowjetunion **3**, 664 (1933).

[2] L. D. Landau, The theory of a fermi liquid, Sov. Phys. JETP **3**, 920 (1957).

[3] A. S. Alexandrov and J. T. Devreese, *Advances in Polaron Physics* (Springer, Berlin, 2010).

[4] S. I. Pekar, Autolocalization of the electron in an inertially polarizable dielectric medium, Zh. Eksp. Teor. Fiz. **16**, 335 (1946).

[5] S. I. Pekar, Theory of colored crystals, Zh. Eksp. Teor. Fiz. **17**, 868 (1947).

[6] L. D. Landau and S. I. Pekar, Effective mass of a polaron, Zh. Eksp. Teor. Fiz. **18**, 419 (1948).

[7] R. P. Feynman, Slow electrons in a polar crystal, Phys. Rev. **97**, 660 (1955).

[8] S. Moser, L. Moreschini, J. Jaćimović, O. S. Barišić, H. Berger, A. Magrez, Y. J. Chang, K. S. Kim, A. Bostwick, E. Rotenberg, L. Forró, and M. Grioni, Tunable Polaronic Conduction in Anatase TiO$_2$, Phys. Rev. Lett. **110**, 196403 (2013).

[9] C. Verdi, F. Caruso, and F. Giustino, Origin of the crossover from polarons to fermi liquids in transition metal oxides, Nat. Commun. **8**, 15769 (2017).

[10] E. Gross, Motion of foreign bodies in boson systems, Ann. Phys. (NY) **19**, 234 (1962).

[11] T. C. Padmore and A. L. Fetter, Impurities in an imperfect bose gas. I. The condensate, Ann. Phys. (NY) **62**, 293 (1971).

[12] I. N. Cherepanov and M. Lemeshko, Fingerprints of angulon instabilities in the spectra of matrix-isolated molecules, Phys. Rev. Mater. **1**, 035602 (2017).

[13] G. Bighin and M. Lemeshko, Diagrammatic approach to orbital quantum impurities interacting with a many-particle environment, Phys. Rev. B **96**, 085410 (2017).

[14] E. Yakaboylu, B. Midya, A. Deuchert, N. Leopold, and M. Lemeshko, Theory of the rotating polaron: Spectrum and self-localization, Phys. Rev. B **98**, 224506 (2018).

[15] J. Catani, G. Lamporesi, D. Naik, M. Gring, M. Inguscio, F. Minardi, A. Kantian, and T. Giamarchi, Quantum dynamics of impurities in a one-dimensional bose gas, Phys. Rev. A **85**, 023623 (2012).

[16] N. Spethmann, F. Kindermann, S. John, C. Weber, D. Meschede, and A. Widera, Dynamics of Single Neutral Impurity Atoms Immersed in an Ultracold Gas, Phys. Rev. Lett. **109**, 235301 (2012).

[17] M. G. Skou, T. G. Skov, N. B. Jørgensen, K. K. Nielsen, A. Camacho-Guardian, T. Pohl, G. M. Bruun, and J. J. Arlt, Non-equilibrium quantum dynamics and formation of the bose polaron, Nat. Phys. **17**, 731 (2021).

[18] Z. Z. Yan, Y. Ni, C. Robens, and M. W. Zwierlein, Bose polarons near quantum criticality, Science **368**, 190 (2020).

[19] M.-G. Hu, M. J. Van de Graaff, D. Kedar, J. P. Corson, E. A. Cornell, and D. S. Jin, Bose Polarons in the Strongly Interacting Regime, Phys. Rev. Lett. **117**, 055301 (2016).

[20] N. B. Jørgensen, L. Wacker, K. T. Skalmstang, M. M. Parish, J. Levinsen, R. S. Christensen, G. M. Bruun, and J. J. Arlt, Observation of Attractive and Repulsive Polarons in a Bose-Einstein Condensate, Phys. Rev. Lett. **117**, 055302 (2016).

[21] H. Fröhlich, Electrons in lattice fields, Adv. Phys. **3**, 325 (1954).

[22] T. Holstein, Studies of polaron motion: Part I. The molecular-crystal model, Ann. Phys. (NY) **8**, 325 (1959).

[23] T. Holstein, Studies of polaron motion: Part II. The "small" polaron, Ann. Phys. (NY) **8**, 343 (1959).

[24] Y.-C. Yam, M. M. Moeller, G. A. Sawatzky, and M. Berciu, Peierls versus Holstein models for describing electron-phonon coupling in perovskites, Phys. Rev. B **102**, 235145 (2020).

[25] W. P. Su, J. R. Schrieffer, and A. J. Heeger, Solitons in Poly-acetylene, Phys. Rev. Lett. **42**, 1698 (1979).

[26] A. J. Heeger, S. Kivelson, J. R. Schrieffer, and W. P. Su, Solitons in conducting polymers, Rev. Mod. Phys. **60**, 781 (1988).

[27] S. Barišić, J. Labbé, and J. Friedel, Tight Binding and Transition-Metal Superconductivity, Phys. Rev. Lett. **25**, 919 (1970).

[28] K. Miyata and X.-Y. Zhu, Ferroelectric large polarons, Nat. Mater. **17**, 379 (2018).

[29] F. Wang, Y. Fu, M. E. Ziffer, Y. Dai, S. F. Maehrlein, and X.-Y. Zhu, Solvated electrons in solids—ferroelectric large polarons in lead halide perovskites, J. Am. Chem. Soc. **143**, 5 (2021).

[30] T. M. Brenner, D. A. Egger, L. Kronik, G. Hodes, and D. Cahen, Hybrid organic—inorganic perovskites: Low-cost semiconductors with intriguing charge-transport properties, Nat. Rev. Mater. **1**, 15007 (2016).

[31] M. B. Johnston and L. M. Herz, Hybrid perovskites for photovoltaics: Charge-carrier recombination, diffusion, and radiative efficiencies, Acc. Chem. Res. **49**, 146 (2016).

[32] A. K. Jena, A. Kulkarni, and T. Miyasaka, Halide perovskite photovoltaics: Background, status, and future prospects, Chem. Rev. **119**, 3036 (2019).

[33] A. Kojima, K. Teshima, Y. Shirai, and T. Miyasaka, Organometal halide perovskites as visible-light sensitizers for photovoltaic cells, J. Am. Chem. Soc. **131**, 6050 (2009).

[34] I. Chung, B. Lee, J. He, R. P. Chang, and M. G. Kanatzidis, All-solid-state dye-sensitized solar cells with high efficiency, Nature (London) **485**, 486 (2012).

[35] M. M. Lee, J. Teuscher, T. Miyasaka, T. N. Murakami, and H. J. Snaith, Efficient hybrid solar cells based on meso-superstructured organometal halide perovskites, Science **338**, 643 (2012).

[36] H.-S. Kim, C.-R. Lee, J.-H. Im, K.-B. Lee, T. Moehl, A. Marchioro, S.-J. Moon, R. Humphry-Baker, J.-H. Yum, J. E. Moser, M. Grätzel, and N.-G. Park, Lead iodide perovskite sensitized all-solid-state submicron thin film mesoscopic solar cell with efficiency exceeding 9%, Sci. Rep. **2**, 591 (2012).

[37] T. Miyasaka, *Perovskite Photovoltaics and Optoelectronics: From Fundamentals to Advanced Applications* (John Wiley & Sons, New York, 2021).

[38] H. Fujiwara, *Hybrid Perovskite Solar Cells: Characteristics and Operation* (John Wiley & Sons, New York, 2022).

[39] K. Miyata, T. L. Atallah, and X.-Y. Zhu, Lead halide per-ovskites: Crystal-liquid duality, phonon glass electron crystals, and large polaron formation, Sci. Adv. **3**, e1701469 (2017).

[40] C. Eames, J. M. Frost, P. R. Barnes, B. C. O'regan, A. Walsh, and M. S. Islam, Ionic transport in hybrid lead iodide per-ovskite solar cells, Nat. Commun. **6**, 7497 (2015).

[41] Y. Yuan and J. Huang, Ion migration in organometal trihalide perovskite and its impact on photovoltaic efficiency and stabil-ity, Acc. Chem. Res. **49**, 286 (2016).

[42] T. Chen, W.-L. Chen, B. J. Foley, J. Lee, J. P. Ruff, J. P. Ko, C. M. Brown, L. W. Harriger, D. Zhang, C. Park, M. Yoon, Y.-M. Chang, J. J. Choi, and S.-H. Lee, Origin of long lifetime of band-edge charge carriers in organic–inorganic lead iodide perovskites, Proc. Natl. Acad. Sci. USA **114**, 7519 (2017).

[43] O. Selig, A. Sadhanala, C. Müller, R. Lovrincic, Z. Chen, Y. L. Rezus, J. M. Frost, T. L. Jansen, and A. A. Bakulin, Organic cation rotation and immobilization in pure and mixed

[44] methylammonium lead-halide perovskites, J. Am. Chem. Soc. **139**, 4068 (2017).

[44] S. Liu, R. Guo, and F. Xie, The effects of organic cation rotation on hybrid organic-inorganic perovskites: A critical review, Mater. Des. **221**, 110951 (2022).

[45] E. M. Mozur and J. R. Neilson, Cation dynamics in hybrid halide perovskites, Annu. Rev. Mater. Res. **51**, 269 (2021).

[46] J. Even, L. Pedesseau, and C. Katan, Analysis of multivalley and multibandgap absorption and enhancement of free carriers related to exciton screening in hybrid perovskites, J. Phys. Chem. C **118**, 11566 (2014).

[47] A. Amat, E. Mosconi, E. Ronca, C. Quarti, P. Umari, M. K. Nazeeruddin, M. Gratzel, and F. De Angelis, Cation-induced band-gap tuning in organohalide perovskites: Interplay of spin–orbit coupling and octahedra tilting, Nano Lett. **14**, 3608 (2014).

[48] J. Even, L. Pedesseau, J.-M. Jancu, and C. Katan, DFT and $\mathbf{k} \cdot \mathbf{p}$ modelling of the phase transitions of lead and tin halide perovskites for photovoltaic cells, Phys. Status Solidi RRL **8**, 31 (2014).

[49] F. Zheng, L. Z. Tan, S. Liu, and A. M. Rappe, Rashba spin–orbit coupling enhanced carrier lifetime in $CH_3NH_3PbI_3$, Nano Lett. **15**, 7794 (2015).

[50] X.-Y. Zhu and V. Podzorov, Charge carriers in hybrid organic–inorganic lead halide perovskites might be protected as large polarons, J. Phys. Chem. Lett. **6**, 4758 (2015).

[51] E. Welch, L. Scolfaro, and A. Zakhidov, Density functional theory + U modeling of polarons in organohalide lead per-ovskites, AIP Adv. **6**, 125037 (2016).

[52] A. J. Neukirch, W. Nie, J.-C. Blancon, K. Appavoo, H. Tsai, M. Y. Sfeir, C. Katan, L. Pedesseau, J. Even, J. J. Crochet, G. Gupta, A. D. Mohite, and S. Tretiak, Polaron stabilization by cooperative lattice distortion and cation rotations in hybrid perovskite materials, Nano Lett. **16**, 3809 (2016).

[53] T. Ivanovska, C. Dionigi, E. Mosconi, F. De Angelis, F. Liscio, V. Morandi, and G. Ruani, Long-lived photoinduced polarons in organohalide perovskites, J. Phys. Chem. Lett. **8**, 3081 (2017).

[54] F. Zheng and L.-w. Wang, Large polaron formation and its effect on electron transport in hybrid perovskites, Energy Environ. Sci. **12**, 1219 (2019).

[55] F. Ambrosio, J. Wiktor, F. De Angelis, and A. Pasquarello, Origin of low electron–hole recombination rate in metal halide perovskites, Energy Environ. Sci. **11**, 101 (2018).

[56] F. Ambrosio, D. Meggiolaro, E. Mosconi, and F. De Angelis, Charge localization, stabilization, and hopping in lead halide perovskites: competition between polaron stabilization and cation disorder, ACS Energy Lett. **4**, 2013 (2019).

[57] F. Wang, W. Chu, L. Huber, T. Tu, Y. Dai, J. Wang, H. Peng, J. Zhao, and X.-Y. Zhu, Phonon signatures for polaron formation in an anharmonic semiconductor, Proc. Natl. Acad. Sci. USA **119**, e2122436119 (2022).

[58] K. Miyata, D. Meggiolaro, M. T. Trinh, P. P. Joshi, E. Mosconi, S. C. Jones, F. De Angelis, and X.-Y. Zhu, Large polarons in lead halide perovskites, Sci. Adv. **3**, e1701217 (2017).

[59] D. Meggiolaro, F. Ambrosio, E. Mosconi, A. Mahata, and F. De Angelis, Polarons in metal halide perovskites, Adv. Energy Mater. **10**, 1902748 (2020).

[60] T. M. Brenner, D. A. Egger, A. M. Rappe, L. Kronik, G. Hodes, and D. Cahen, Are mobilities in hybrid

organic–inorganic halide perovskites actually "high"? J. Phys. Chem. Lett. **6**, 4754 (2015).

[61] H. Zhu, K. Miyata, Y. Fu, J. Wang, P. P. Joshi, D. Niesner, K. W. Williams, S. Jin, and X.-Y. Zhu, Screening in crystalline liquids protects energetic carriers in hybrid perovskites, Science **353**, 1409 (2016).

[62] Y. Rakita, O. Bar-Elli, E. Meirzadeh, H. Kaslasi, Y. Peleg, G. Hodes, I. Lubomirsky, D. Oron, D. Ehre, and D. Cahen, Tetragonal CH$_3$NH$_3$PbI$_3$ is ferroelectric, Proc. Natl. Acad. Sci. USA **114**, E5504 (2017).

[63] S. Shahrokhi, W. Gao, Y. Wang, P. R. Anandan, M. Z. Rahaman, S. Singh, D. Wang, C. Cazorla, G. Yuan, J.-M. Liu, and T. Wu, Emergence of ferroelectricity in halide perovskites, Small Methods **4**, 2000149 (2020).

[64] Y. Liu, L. Collins, R. Proksch, S. Kim, B. R. Watson, B. Doughty, T. R. Calhoun, M. Ahmadi, A. V. Ievlev, S. Jesse, S. T. Retterer, A. Belianinov, K. Xiao, J. Huang, B. G. Sumpter, S. V. Kalinin, B. Hu, and O. S. Ovchinnikova, Chemical nature of ferroelastic twin domains in CH$_3$NH$_3$PbI$_3$ perovskite, Nat. Mater. **17**, 1013 (2018).

[65] A. S. Alexandrov and B. Y. Yavidov, Small adiabatic polaron with a long-range electron-phonon interaction, Phys. Rev. B **69**, 073101 (2004).

[66] O. R. Tozer and W. Barford, Localization of large polarons in the disordered Holstein model, Phys. Rev. B **89**, 155434 (2014).

[67] N. K. Tailor and S. Satapathi, Anisotropy in perovskite single crystals: From fundamentals to applications, J. Phys. Chem. C **126**, 17789 (2022).

[68] A. S. Baimuratov, T. P. Pereziabova, W. Zhu, M. Y. Leonov, A. V. Baranov, A. V. Fedorov, and I. D. Rukhlenko, Optical anisotropy of topologically distorted semiconductor nanocrystals, Nano Lett. **17**, 5514 (2017).

[69] Y. Jiao, S. Yi, H. Wang, B. Li, W. Hao, L. Pan, Y. Shi, X. Li, P. Liu, H. Zhang, C. Gao, J. Zhao, and J. Lu, Strain engineering of metal halide perovskites on coupling anisotropic behaviors, Adv. Funct. Mater. **31**, 2006243 (2021).

[70] D. H. Fabini, T. A. Siaw, C. C. Stoumpos, G. Laurita, D. Olds, K. Page, J. G. Hu, M. G. Kanatzidis, S. Han, and R. Seshadri, Universal dynamics of molecular reorientation in hybrid lead iodide perovskites, J. Am. Chem. Soc. **139**, 16875 (2017).

[71] O. Yaffe, Y. Guo, L. Z. Tan, D. A. Egger, T. Hull, C. C. Stoumpos, F. Zheng, T. F. Heinz, L. Kronik, M. G. Kanatzidis, J. S. Owen, A. M. Rappe, M. A. Pimenta, and L. E. Brus, Local Polar Fluctuations in Lead Halide Perovskite Crystals, Phys. Rev. Lett. **118**, 136001 (2017).

[72] F. Giustino, Electron-phonon interactions from first principles, Rev. Mod. Phys. **89**, 015003 (2017).

[73] M. Z. Mayers, L. Z. Tan, D. A. Egger, A. M. Rappe, and D. R. Reichman, How lattice and charge fluctuations control carrier dynamics in halide perovskites, Nano Lett. **18**, 8041 (2018).

[74] A. G. Volosniev, A. Shiva Kumar, D. Lorenc, Y. Ashourishokri, A. A. Zhumekenov, O. M. Bakr, M. Lemeshko, and Z. Alpichshev, Spin-Electric Coupling in Lead Halide Perovskites, Phys. Rev. Lett. **130**, 106901 (2023).

[75] A. G. Volosniev, A. S. Kumar, D. Lorenc, Y. Ashourishokri, A. A. Zhumekenov, O. M. Bakr, M. Lemeshko, and Z. Alpichshev, Effective model for studying optical properties of lead halide perovskites, Phys. Rev. B **107**, 125201 (2023).

[76] A. Lacroix, G. T. de Laissardière, P. Quémerais, J.-P. Julien, and D. Mayou, Modeling of Electronic Mobilities in Halide Perovskites: Adiabatic Quantum Localization Scenario, Phys. Rev. Lett. **124**, 196601 (2020).

[77] J. Kang and L.-W. Wang, Dynamic disorder and potential fluctuation in two-dimensional perovskite, J. Phys. Chem. Lett. **8**, 3875 (2017).

[78] I. G. Lang and Y. A. Firsov, Mobility of small-radius polarons at low temperatures, Zh. Eksp. Teor. Fiz. **45**, 378 (1963) [Sov. Phys. JETP **18**, 262 (1964)].

[79] F. Grusdt and E. Demler, New theoretical approaches to bose polarons, *Quantum Matter Ultralow Temperatures*, edited by M. Inguscio, S. Stringari, W. Ketterle, and G. Roati (IOS press, Amsterdam, 2015), pp. 325–411.

[80] H. Spohn, Roughening and pinning transitions for the polaron, J. Phys. A **19**, 533 (1986).

[81] B. Gerlach and H. Löwen, Analytical properties of polaron systems or: Do polaronic phase transitions exist or not? Rev. Mod. Phys. **63**, 63 (1991).

[82] S. D. Stranks, G. E. Eperon, G. Grancini, C. Menelaou, M. J. P. Alcocer, T. Leijtens, L. M. Herz, A. Petrozza, and H. J. Snaith, Electron-hole diffusion lengths exceeding 1 micrometer in an organometal trihalide perovskite absorber, Science **342**, 341 (2013).

[83] D. Shi, V. Adinolfi, R. Comin, M. Yuan, E. Alarousu, A. Buin, Y. Chen, S. Hoogland, A. Rothenberger, K. Katsiev, Y. Losovyj, X. Zhang, P. A. Dowben, O. F. Mohammed, E. H. Sargent, and O. M. Bakr, Low trap-state density and long carrier diffusion in organolead trihalide perovskite single crystals, Science **347**, 519 (2015).

[84] Q. Dong, Y. Fang, Y. Shao, P. Mulligan, J. Qiu, L. Cao, and J. Huang, Electron-hole diffusion lengths $>175\,\mu m$ in solution-grown CH$_3$NH$_3$PbI$_3$ single crystals, Science **347**, 967 (2015).

[85] S. Poncé, M. Schlipf, and F. Giustino, Origin of low carrier mobilities in halide perovskites, ACS Energy Lett. **4**, 456 (2019).

[86] M. B. Price, J. Butkus, T. C. Jellicoe, A. Sadhanala, A. Briane, J. E. Halpert, K. Broch, J. M. Hodgkiss, R. H. Friend, and F. Deschler, Hot-carrier cooling and photoinduced refractive index changes in organic–inorganic lead halide perovskites, Nat. Commun. **6**, 8420 (2015).

[87] M. Sajedi, M. Krivenkov, D. Marchenko, J. Sánchez-Barriga, A. K. Chandran, A. Varykhalov, E. D. L. Rienks, I. Aguilera, S. Blügel, and O. Rader, Is There a Polaron Signature in Angle-Resolved Photoemission of CsPbBr$_3$? Phys. Rev. Lett. **128**, 176405 (2022).

[88] B. Guzelturk, T. Winkler, T. W. J. Van de Goor, M. D. Smith, S. A. Bourelle, S. Feldmann, M. Trigo, S. W. Teitelbaum, H.-G. Steinrück, G. A. de la Pena, R. Alonso-Mori, D. Zhu, T. Sato, H. I. Karunadasa, M. F. Toney, F. Deschler, and A. M. Lindenberg, Visualization of dynamic polaronic strain fields in hybrid lead halide perovskites, Nat. Mater. **20**, 618 (2021).

[89] D. Bao, Q. Chang, B. Chen, X. Chen, H. Sun, Y. M. Lam, D. Zhao, J.-X. Zhu, and E. E. M. Chia, Evidence of polaron formation in halide perovskites via carrier effective mass measurements, PRX Energy **2**, 013001 (2023).

[90] E. Jeckelmann and S. R. White, Density-matrix renormalization-group study of the polaron problem in the Holstein model, Phys. Rev. B **57**, 6376 (1998).

[91] J. Even, L. Pedesseau, C. Katan, M. Kepenekian, J.-S. Lauret, D. Sapori, and E. Deleporte, Solid-state physics perspective on hybrid perovskite semiconductors, J. Phys. Chem. C **119**, 10161 (2015).

[92] S. Yun, X. Zhou, J. Even, and A. Hagfeldt, Theoretical treatment of $CH_3NH_3PbI_3$ perovskite solar cells, Angew. Chem. Int. Ed. **56**, 15806 (2017).

[93] B. Traoré, J. Even, L. Pedesseau, M. Kepenekian, and C. Katan, Band gap, effective masses, and energy level alignment of 2D and 3D halide perovskites and heterostructures using DFT-1/2, Phys. Rev. Mater. **6**, 014604 (2022).

[94] R. Jinnouchi, J. Lahnsteiner, F. Karsai, G. Kresse, and M. Bokdam, Phase Transitions of Hybrid Perovskites Simulated by Machine-Learning Force Fields Trained on the Fly with Bayesian Inference, Phys. Rev. Lett. **122**, 225701 (2019).

[95] L. Zhang, M. He, and S. Shao, Machine learning for halide perovskite materials, Nano Energy **78**, 105380 (2020).

[96] C. W. Myung, A. Hajibabaei, J.-H. Cha, M. Ha, J. Kim, and K. S. Kim, Challenges, opportunities, and prospects in metal halide perovskites from theoretical and machine learning perspectives, Adv. Energy Mater. **12**, 2202279 (2022).

[97] L. Pitaevskii and S. Stringari, *Bose-Einstein Condensation and Superfluidity*, International Series of Monographs on Physics (Oxford University Press, Oxford, 2016).

[98] S. Boyer-Richard, C. Katan, B. Traoré, R. Scholz, J.-M. Jancu, and J. Even, Symmetry-based tight binding modeling of halide perovskite semiconductors, J. Phys. Chem. Lett. **7**, 3833 (2016).

[99] R. Schmidt and M. Lemeshko, Rotation of Quantum Impurities in the Presence of a Many-Body Environment, Phys. Rev. Lett. **114**, 203001 (2015).

[100] R. Schmidt and M. Lemeshko, Deformation of a Quantum Many-Particle System by a Rotating Impurity, Phys. Rev. X **6**, 011012 (2016).

[101] E. Yakaboylu and M. Lemeshko, Anomalous Screening of Quantum Impurities by a Neutral Environment, Phys. Rev. Lett. **118**, 085302 (2017).

[102] Y. Cui, Y.-Y. Liu, J.-P. Deng, X.-Z. Zhang, R.-B. Yang, Z.-Q. Li, and Z.-W. Wang, Microscopic theory of Raman scattering for the rotational organic cation in metal halide perovskites, Phys. Rev. B **107**, 094306 (2023).

[103] J.-W. Wu, Y. Cui, S.-J. Li, and Z.-W. Wang, Optical absorption of angulon in metal halide perovskites, arXiv:2212.06356.

[104] *Handbook of Mathematical Functions*, edited by M. Abramowitz and I. A. Stegun, Dover Books on Mathematics (Dover Publications, Mineola, NY, 1965).

[105] P. A. M. Dirac, On the annihilation of electrons and protons, Proc. Cambridge Philos. Soc. **26**, 361 (1930).

[106] J. Frenkel, *Wave Mechanics, Advanced General Theory*, Vol. 1 (Oxford University Press, Oxford, 1934).

[107] M. Beck, A. Jäckle, G. Worth, and H.-D. Meyer, The multiconfiguration time-dependent hartree (MCTDH) method: A highly efficient algorithm for propagating wavepackets, Phys. Rep. **324**, 1 (2000).

[108] P. Kramer and M. Saraceno, *Geometry of the Time-dependent Variational Principle in Quantum Mechanics*, Lecture Notes in Physics (Springer-Verlag, Berlin, 1981).

[109] H.-J. Kull and D. Pfirsch, Generalized variational principle for the time-dependent Hartree-Fock equations for a Slater determinant, Phys. Rev. E **61**, 5940 (2000).

[110] A. D. McLachlan, A variational solution of the time-dependent schrodinger equation, Mol. Phys. **8**, 39 (1964).

[111] J. Broeckhove, L. Lathouwers, E. Kesteloot, and P. Van Leuven, On the equivalence of time-dependent variational principles, Chem. Phys. Lett. **149**, 547 (1988).

[112] D. Thouless, Stability conditions and nuclear rotations in the Hartree-Fock theory, Nucl. Phys. **21**, 225 (1960).

[113] I. Hubač and S. Wilson, Brillouin-Wigner perturbation theory, in *Brillouin-Wigner Methods for Many-Body Systems* (Springer Netherlands, Dordrecht, 2010), pp. 37–68.

[114] F. Chevy, Universal phase diagram of a strongly interacting Fermi gas with unbalanced spin populations, Phys. Rev. A **74**, 063628 (2006).

[115] F. Scazza, G. Valtolina, P. Massignan, A. Recati, A. Amico, A. Burchianti, C. Fort, M. Inguscio, M. Zaccanti, and G. Roati, Repulsive Fermi Polarons in a Resonant Mixture of Ultracold ^{6}Li Atoms, Phys. Rev. Lett. **118**, 083602 (2017).

[116] C. Kohstall, M. Zaccanti, M. Jag, A. Trenkwalder, P. Massignan, G. M. Bruun, F. Schreck, and R. Grimm, Metastability and coherence of repulsive polarons in a strongly interacting Fermi mixture, Nature (London) **485**, 615 (2012).

[117] A. Schirotzek, C.-H. Wu, A. Sommer, and M. W. Zwierlein, Observation of Fermi Polarons in a Tunable Fermi Liquid of Ultracold Atoms, Phys. Rev. Lett. **102**, 230402 (2009).

[118] M. Cetina, M. Jag, R. S. Lous, I. Fritsche, J. T. M. Walraven, R. Grimm, J. Levinsen, M. M. Parish, R. Schmidt, M. Knap, and E. Demler, Ultrafast many-body interferometry of impurities coupled to a fermi sea, Science **354**, 96 (2016).